Image Reconstruction by means of Kalman Filtering in Passive Millimetre-Wave Imaging

D. MP Smith[1*], P. Meyer[1], B. M Herbst[2]

[1]Department of Electrical and Electronic Engineering, University of Stellenbosch, Private Bag X1, Matieland 7602, Stellenbosch, South Africa
parick@sun.ac.za
[2]Division of Applied Mathematics, Department of Mathematics, University of Stellenbosch, Private Bag X1, Matieland 7602, Stellenbosch, South Africa
herbst@sun.ac.za
*Corresponding author

Abstract

Passive millimetre-wave (PMMW) imaging is a technique that detects thermal radiation emitted and reflected by metallic and non-metallic objects. While visual and infra-red (IR) emissions are attenuated by atmospheric constituents, PMMW emissions are transmitted, resulting in consistent contrast between objects from day to night even in low-visibility conditions. The use of a PMMW imaging system on an unmanned aerial vehicle (UAV) has applications for airborne surveillance, but the size of the UAV precludes optical or mechanical scanning. One solution is a long, thin antenna fitted under the UAV. This antenna has a narrow beam along the plane perpendicular to the flight path, but a broad beam along the plane of the flight path blurs the image, making it difficult to determine the position of objects or to differentiate between objects. This paper proposes a technique of image reconstruction based on the Kalman filter to reconstruct an accurate image of the target area from such a detected signal. It is shown that given a simulated target area, the Kalman filter is able to reconstruct the image using the measured antenna pattern to model the scanning process and reverse the blurring effect.

Keywords: Image Reconstruction, Kalman Filter, Passive Millimetre-Wave Imaging

1. Introduction

Passive millimetre-wave (PMMW) imaging is a technique that uses radiometers to detect thermal radiation emitted and reflected by metallic and non-metallic objects. While visual and infra-red (IR) emissions are attenuated by atmospheric constituents, PMMW emissions are transmitted, resulting in consistent contrast between objects from day to night even in low-visibility conditions to form images for a range of security and inclement weather applications.

Passive imaging techniques form images by exploiting the natural phenomena of objects within a target area and the medium surrounding the target area. The effective temperature of an object is a function of emission of physical temperature, reflection of illumination temperature

and transmission of background temperature. The detected temperature of an object is the effective temperature of the medium, with the object supplying the background temperature.

In clear weather the use of optical radiometers to detect the reflected illumination off objects in the presence of sunlight and the use of IR radiometers to detect the emitted radiation of objects in the absence of sunlight are sufficient to form an image of the target area. The presence of atmospheric constituents within the medium separating the radiometer from the target area causes sufficient attenuation to cripple these imaging systems.

PMMW imaging systems operate within the millimetre-wave (MMW) region, defined as $30\,GHz$ to $300\,GHz$. Imaging within the MMW region in inclement weather is possible because the MMW region contains transmission windows around $35\,GHz$, $94\,GHz$, $140\,GHz$ and $220\,GHz$, where the attenuation caused by atmospheric constituents such as oxygen, precipitation, suspended water particles and water vapour is low (Liebe 1983).

The unique difference in signature in the MMW region between metallic objects, detected by strongly reflecting the illumination temperature, and non-metallic objects, detected by strongly emitting the physical temperature, result in high contrast images (Yujiri 2003). For a large range of atmospheric conditions even camouflaged metallic objects are distinguishable from the surrounding absorptive background (Wilson 1986).

The concentration of natural illumination within the optical region, the concentration of natural emissions within the IR region and the minimal variation in transmission between different atmospheric constituents within the transmission windows of the MMW region result in PMMW images that have consistent contrast between different objects from day to night in clear weather and in low visibility conditions.

These images are used in all-weather fixed and mobile land, air and sea surveillance and navigation (Wilson 1986, Appleby 2007), such as the location and point of origin of boats in search and rescue operations, for reconnaissance and in the apprehension of drug traffickers (Yujiri 2003). The transmission of MMW emissions through canvas and plastic is used to detect concealed personnel in soft-sided vehicles attempting to illegally cross borders (Hopper 2005).

The contrast in emission between land, water, vegetation and minerals results in the identification of planetary surface composition to allow for mapping of annual rainfall levels (Chandrasekar 2003) and the degree of moisture in agricultural land (Ulaby 1986, §19.1). The extent of the change in emission of water caused by the introduction of oil and ice is used to map the extent and thickness of an oil spill at sea (Yujiri 2003) and map sea ice movements (Ulaby 1986, §18.5).

The use of a PMMW imaging system on a unmanned aerial vehicle (UAV) has applications for airborne surveillance, but the size of the UAV precludes optical or mechanical scanning. One solution is a long, thin antenna fitted under the UAV. This antenna has a narrow beam along the plane perpendicular to the flight path, but a broad beam along the plane of the flight path blurs the image, making it difficult to determine the position of objects or to differentiate between objects.

This paper proposes a technique of image reconstruction based on the Kalman filter (Kalman 1960), a recursive filter that uses feedback control to estimate the state of a partially observed process, to reconstruct an accurate image of the target area from the detected signal. Given a simulated target area, the Kalman filter is able to reconstruct the image using the measured antenna pattern to model the scanning process and reverse the blurring effect.

In Section 2 the passive imaging system is designed, showing how the image is formed. In Section 3 the mathematical model of the Kalman filter is detailed, showing how the image is

reconstructed from noisy measurements. In Section 4 the implemented system is described, showing how the parameters are assigned for the given system. In Section 5 simulated results of the proposed technique are dissected, showing how the Kalman filter reconstructs the image.

2. PMMW Imaging System

In this paper a PMMW imaging system, designed to detect objects in low-visibility conditions, is proposed for fitting under a UAV. PMMW images are formed by capturing the emissions from the target area using antennae and measuring the magnitude of the captured emissions with detectors. The simplest model is a single antenna operating at a single frequency directed at a single orientation scanned over the target area by a mechanical motor, as depicted in Fig 1.
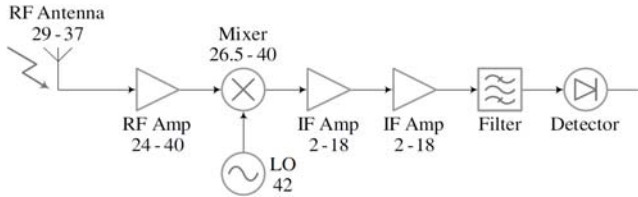

Fig. 1. Total power peterodyne radiometer

The antenna captures the emissions, the mixer converts the radio frequency (RF) f_{RF} signal to a lower intermediate frequency (IF) f_{IF} signal using the local oscillator (LO) frequency f_{LO}, the filter removes the unwanted mixing products and the detector converts the wanted signal to a power level, with the amplifiers strengthening the signal. Good noise performance is vital to deal with the emissions that are between 10^{10} and 10^{7} times smaller than IR emissions.

The choice of atmospheric window is a compromise between price, transmission and resolution. Technology is immature within the transmission windows at $140GHz$ and $220GHz$, thereby making these options not cost-effective. For a given antenna aperture the $94GHz$ window has greater spatial resolution, but the $35GHz$ window is chosen for the greater transmission through atmospheric constituents and thin layers of absorbent materials.

The speed of the simple model of Fig. 1 is increased by making use of multiple antennae, with the orientation of the antennae controlled using electronic, optical or mechanical techniques. The size of the UAV precludes any form of optical or mechanical scanning, thereby limiting the design to electronic scanning. In using the motion of the UAV to scan along the plane of the flight path, the antenna scans only along the plane perpendicular to the flight path.

As the phase of the antenna tilts linearly as a function of frequency, by measuring the antenna over a wide frequency band the scan angle is swept over the target area. Frequency-scanning arrays are simple, inexpensive and reliable as no expensive controlling electronics and no slow moving parts are required, with space-to-frequency mapping an inherent property, as depicted in Fig. 2. While the scan angle is limited, this is an economical, compact and fast system well suited to work with the available space and power on the UAV.
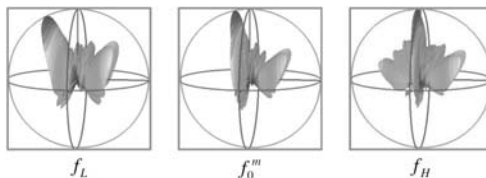
Fig. 2. Antenna patterns at different frequencies

In using a frequency-scanned array for the antenna the captured emissions are split up into different frequency bands before detection to maintain the space-to-frequency mapping of the antenna. This is done by upgrading the simple model of Fig. 1 to include a multiplexer after the second IF amplifier and adding a filter and detector for each channel of the multiplexer, as depicted in Fig. 3.
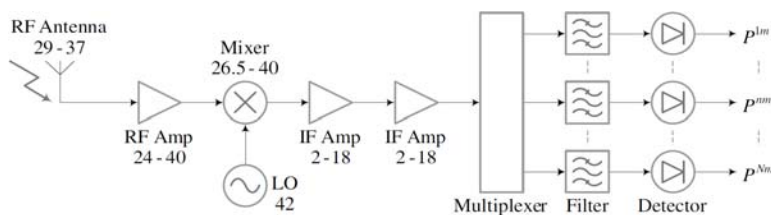

Fig. 3. Multi-channel passive millimetre-wave imaging radiometer

The spatial resolution of an imaging system is defined by the number of resolvable pixels across the horizontal field of view, and is directly proportional to the size of the antenna and indirectly proportional to the wavelength of the emissions. MMW wavelengths are much longer than optical and IR wavelengths, requiring much larger antennae to achieve equivalent resolution to IR and optical imaging systems.

The image is built up line by line as the antenna concurrently scans the target area along the plane perpendicular to the flight path, with each orientation scanned by a beam at a different frequency f_0^m. The frequency range f_L to f_H is divided into M contiguous bands, each assigned to a different pixel column, P^m. The flight path time-period t_0 to t_N is divided into N measurements taken at discrete time-intervals, each assigned to a different pixel row, P^n.

The combination of flight-measuring and scan-filtering maps the $w \times h$ coordinate system of the target area to the $f \times t$ coordinate system of the image of size $N \times M$, as depicted in Fig. 4. Because of the antenna construction, it displays a narrow, high gain, frequency-scanned beam along the plane perpendicular to the flight path, but a very broad beam along the plane of the flight path that leads to a larger area than the target area being detected.
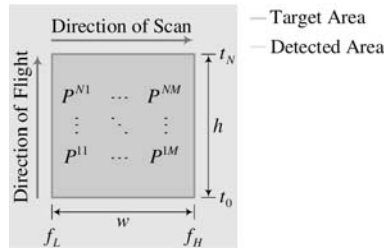
Fig. 4. Target area

When flying over the target area the image of an object is blurred along the plane of the flight path, making it difficult to determine the position of objects or to differentiate between objects situated along the plane of the flight path. Prevention is impossible as the size of the UAV precludes the use of bulky optics to focus the antenna along the plane of the flight path as well. The solution is a post-processor that reconstructs the target area from the blurred image.

3. Mathematical Model

Image degradation is conventionally defined in literature as a combination of blurring of the edges between regions and the addition of random noise to the image. The conventional methodology of image reconstruction is to invert the effect of the degradation. As blurring and noising have opposing effects, the reconstruction algorithm must balance deblurring and denoising to reconstruct the original image.

The conventional methodology makes use of algorithms incorporating iterative partial differential equations of the form $z_{k+1} = z_k + \Delta t \partial z_k / \partial t$, where Δt is the step size of the algorithm and the reconstruction method is determined by the formulation of $\partial z_k / \partial t$. There are three basic approaches to reconstruct an image, with the two denoising algorithm based on parabolic equations and the deblurring algorithm based on hyperbolic equations.

The canonical axiomatic approach to denoising is isotropic diffusion, which is equivalent to a smoothing process with a Gaussian kernel. Isotropic diffusion contains no mechanism to differentiate between regions in an image and diffuses the image as a whole. Anisotropic diffusion (Perona 1990) was introduced in order to locate and diffuse regions separately while maintaining sharp edges by constructing a nonlinear adaptive denoising process.

The canonical variational approach to denoising is total variation (Rudin 1992), which is a minimisation process. Total variation uses a globally defined scalar, λ, that results in fine detail being diffused. Adaptive total variation (Gilboa 2003) was introduced in order to preserve texture by locally reformulating λ. The locally defined λ results in each region being denoised separately to improve the detail retention during denoising.

The canonical approach to deblurring is the shock filter (Osher 1990), which behaves similar to deconvolution. The edges are sharpened by developing shocks at inflection points. The shock filter is sensitive to noise as noise adds inflection points to the image, disrupting the process and resulting in noise in the image being enhanced. The combination of diffusion and the shock filter was introduced in order to increase robustness to noise (Alvarez 1994).

A perfect imaging system has a beam focused on a portion of landmass equal in size to a pixel, resulting in a one-to-one relationship between the target area and the detected image. However, no imaging system is perfect. Conventional blurring caused by an imperfectly

focused lens smoothes an image's edges between regions, as depicted in Fig. 5. Conventional blurring is localised as only the surrounding area is incorporated into the image.
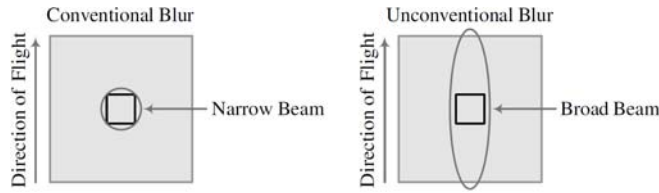

Fig. 5. Image blur

In the proposed application the blurring problem is magnified as there is a many-to-one relationship between the target area and the detected signal due to the broad beam of the antenna. Each pixel of the image incorporates data from within the target area and outside of the target area, as depicted in Fig. 5. Conventional techniques cannot be used as they deal with localised object blurring, which is unable to counter the global object blurring of the antenna.

The Kalman filter is a set of mathematical equations that estimate a process by using feedback control. The time update equations projecting forward in time the current state estimate to the next time step and then the measurement update equations obtain feedback in the form of noisy measurements to adjust the projected estimate to obtain an improved estimate.

The non-stationary, discrete-time, linear process $\mathbf{x}_{k+1} \in \Re^n$ is modelled as

$$\mathbf{x}_{k+1} = \mathbf{A}_k \mathbf{x}_k + \mathbf{B}_k \mathbf{u}_k + \mathbf{v}_k \tag{1}$$

where $\mathbf{u}_k \in \Re^l$ is the external control that drives the process from state $\mathbf{x}_k$ to state $\mathbf{x}_{k+1}$, $\mathbf{v}_k$ is the process noise, $n \times n$ matrix $\mathbf{A}_k$ relates state $\mathbf{x}_k$ to state $\mathbf{x}_{k+1}$ in the absence of both external control $\mathbf{u}_k$ and process noise $\mathbf{v}_k$ and $n \times l$ matrix $\mathbf{B}_k$ relates external control $\mathbf{u}_k$ to state $\mathbf{x}_k$.

State $\mathbf{x}_k$ is accessible from the noise contaminated measurement $\mathbf{z}_k \in \Re^m$ modelled as

$$\mathbf{z}_k = \mathbf{H}_k \mathbf{x}_k + \mathbf{w}_k \tag{2}$$

where $\mathbf{w}_k$ is the measurement noise and $m \times n$ matrix $\mathbf{H}_k$ relates state $\mathbf{x}_k$ to measurement $\mathbf{z}_k$.

Process noise $\mathbf{v}_k$ and measurement noise $\mathbf{w}_k$ are independent of each other, additive, zero-mean, white and Gaussian with normal probability distributions

$$\begin{aligned} p(\mathbf{v}_k) &\sim \mathcal{N}(\mathbf{0}, \mathbf{Q}_k) \\ p(\mathbf{w}_k) &\sim \mathcal{N}(\mathbf{0}, \mathbf{R}_k) \end{aligned} \tag{3}$$

where $\mathbf{Q}_k = E[\mathbf{v}_k \mathbf{v}_k^T]$ is the process noise covariance, $\mathbf{R}_k = E[\mathbf{w}_k \mathbf{w}_k^T]$ is the measurement noise covariance and $E[\mathbf{v}_k \mathbf{v}_n^T] = 0 = E[\mathbf{w}_k \mathbf{w}_n^T], n \neq k$.

A priori estimate $\mathbf{x}_{k+1|k} \in \Re^n$ of state $\mathbf{x}_{k+1}$ is given by the expectation

$$\mathbf{x}_{k+1|k} = E[\mathbf{x}_{k+1} | \mathbf{Z}^k] \tag{4}$$

where $\mathbf{x}_{i|j}, i \geq j$ is the estimate of state $\mathbf{x}_i$ using measurements $\mathbf{Z}^j = \{\mathbf{z}_0, \ldots, \mathbf{z}_j\}$ up to and including time j and is obtained from the noise-free version of the process model of (1), a posteriori state estimate $\mathbf{x}_{k|k}$ and external control $\mathbf{u}_k$.

A posteriori state estimate $\mathbf{x}_{k+1|k+1} \in \mathfrak{R}^n$ is obtained from a priori state estimate $\mathbf{x}_{k+1|k}$ and the weighted difference between measurement $\mathbf{z}_{k+1}$ and a priori measurement estimate $\mathbf{z}_{k+1|k}$

$$\mathbf{x}_{k+1|k+1} \quad = \quad \mathbf{x}_{k+1|k} + \mathbf{K}_{k+1}(\mathbf{z}_{k+1} - \mathbf{z}_{k+1|k}) \tag{5}$$

where $n \times m$ matrix $\mathbf{K}_{k+1}$ is the Kalman gain. Kalman gain $\mathbf{K}_{k+1}$ is the optimal linear estimator that minimises a posteriori error covariance $\mathbf{P}_{k+1|k+1}$.

A priori state error covariance $\mathbf{P}_{k+1|k}$ is obtained from a priori state estimate $\mathbf{x}_{k+1|k}$

$$\mathbf{P}_{k+1|k} \quad = \quad \mathbf{A}_k \mathbf{P}_{k|k} \mathbf{A}_k^T + \mathbf{Q}_k \tag{6}$$

where $\mathbf{e}_{k+1|k} = \mathbf{x}_{k+1} - \mathbf{x}_{k+1|k}$ is the a priori state estimation error.

A posteriori state error covariance $\mathbf{P}_{k+1|k+1}$ is obtained from a posteriori state estimate $\mathbf{x}_{k+1|k+1}$

$$\mathbf{P}_{k+1|k+1} \quad = \quad \mathbf{P}_{k+1|k} - \mathbf{P}_{k+1|k}\mathbf{H}_{k+1}^T\mathbf{K}_{k+1}^T - \mathbf{K}_{k+1}\mathbf{H}_{k+1}\mathbf{P}_{k+1|k} + \mathbf{K}_{k+1}(\mathbf{H}_{k+1}\mathbf{P}_{k+1|k}\mathbf{H}_{k+1}^T + \mathbf{R}_{k+1})\mathbf{K}_{k+1}^T \tag{7}$$

where $\mathbf{e}_{k+1|k+1} = \mathbf{x}_{k+1} - \mathbf{x}_{k+1|k+1}$ is the a posteriori state estimation error.

Making the derivative of a posteriori error covariance $\mathbf{P}_{k+1|k+1}$ with respect to Kalman gain $\mathbf{K}_{k+1}$ equal to $\mathbf{0}$ and solving for $\mathbf{K}_{k+1}$ the optimal gain for a posteriori state estimate $\mathbf{x}_{k+1|k+1}$ is

$$\mathbf{K}_{k+1} \quad = \quad \mathbf{P}_{k+1|k}\mathbf{H}_{k+1}^T(\mathbf{H}_{k+1}\mathbf{P}_{k+1|k}\mathbf{H}_{k+1}^T + \mathbf{R}_{k+1})^{-1} \tag{8}$$

which reduces a posteriori state error covariance $\mathbf{P}_{k+1|k+1}$ of (7) to the well known form

$$\mathbf{P}_{k+1|k+1} \quad = \quad \mathbf{P}_{k+1|k} - \mathbf{K}_{k+1}\mathbf{H}_{k+1}\mathbf{P}_{k+1|k} \tag{9}$$

The recursion of a posteriori state error covariance $\mathbf{P}_{k+1|k+1}$ of (9) is ill-conditioned (Andrade-Cetto2005). As the filter converges, the cancelling of significant digits on a posteriori state error covariance $\mathbf{P}_{k+1|k+1}$ leads to asymmetries or to a non positive semi definite (PSD) matrix, which cannot be true from the definition of a posteriori state error covariance $\mathbf{P}_{k+1|k+1}$. Therefore a posteriori state error covariance $\mathbf{P}_{k+1|k+1}$ of (9) is replaced by the Joseph form

$$\mathbf{P}_{k+1|k+1} \quad = \quad (\mathbf{I} - \mathbf{K}_{k+1}\mathbf{H}_{k+1})\mathbf{P}_{k+1|k}(\mathbf{I} - \mathbf{K}_{k+1}\mathbf{H}_{k+1})^T + \mathbf{K}_{k+1}\mathbf{R}_{k+1}\mathbf{K}_{k+1}^T \tag{10}$$

which is PSD given its quadratic nature.

For an uncertain measurement $\mathbf{z}_{k+1}$ and precise a priori state estimate $\mathbf{x}_{k+1|k}$ the prediction of a posteriori state estimate $\mathbf{x}_{k+1|k+1}$ relies more on the process model of (1) than measurement $\mathbf{z}_{k+1}$ and a posteriori state error covariance $\mathbf{P}_{k+1|k+1}$ sees little reduction

$$\lim_{\mathbf{P}_{k+1|k} \to \mathbf{0}} \mathbf{K}_{k+1} = \mathbf{0} \Rightarrow \begin{array}{rcl} \mathbf{x}_{k+1|k+1} &=& \mathbf{x}_{k+1|k} \\ \mathbf{P}_{k+1|k+1} &=& \mathbf{P}_{k+1|k} \end{array} \tag{11}$$

For a precise measurement $\mathbf{z}_{k+1}$ and uncertain a priori state estimate $\mathbf{x}_{k+1|k}$ the prediction of a posteriori state estimate $\mathbf{x}_{k+1|k+1}$ relies more on measurement $\mathbf{z}_{k+1}$ than the process model of (1) and a posteriori state error covariance $\mathbf{P}_{k+1|k+1}$ is considerably reduced

$$\lim_{\mathbf{R}_{k+1} \to \mathbf{0}} \mathbf{K}_{k+1} = \mathbf{H}_{k+1}^{-1} \Rightarrow \begin{array}{rcl} \mathbf{x}_{k+1|k+1} &=& \mathbf{H}_{k+1}^{-1}\mathbf{z}_{k+1} \\ \mathbf{P}_{k+1|k+1} &=& \mathbf{0} \end{array} \tag{12}$$

The Kalman filter works because the combination of a priori state estimate $\mathbf{x}_{k+1|k}$ conditioned on measurements $\mathbf{Z}^k$ and a posteriori state estimate $\mathbf{x}_{k|k}$, with state $\mathbf{x}_k$ distribution

$$p(\mathbf{x}_k \mid \mathbf{z}_k) \sim \mathcal{N}(\mathbf{x}_{k|k}, \mathbf{P}_{k|k}) \tag{13}$$

into a posteriori state estimate $\mathbf{x}_{k+1|k+1}$ is an improved estimate of state $\mathbf{x}_{k+1}$, based on the probability principle that a more accurate estimate is obtained from the combination of two estimates, $(\mathbf{P}_{k+1|k+1}^2)^{-1} = (\mathbf{P}_{k+1|k}^2)^{-1} + (\mathbf{P}_{k|k}^2)^{-1}$.

4. Implementation

For the proposed application of airborne surveillance for search and rescue operations, the antenna is fitted under a UAV flying over the ocean. The target area is assumed to be a constant distance from the UAV and consist only of sea water at a uniform temperature. The only discrepancy from this continuum is the sea vessels being searched for. Reconstruction of the target area is required to determine the position of objects and to differentiate between objects.

For this proposal state $\mathbf{x}_k$ is the target area, process evolution $\mathbf{A}_k$ models the change of the target area due to the flight of the UAV, measurement $\mathbf{z}_k$ is the antenna output and measurement evolution $\mathbf{H}_k$ models the measured antenna pattern. The change from state $\mathbf{x}_k$ to state $\mathbf{x}_{k+1}$ is based entirely on the flight of the UAV, reducing the process model of (1) to

$$\mathbf{x}_{k+1} = \mathbf{A}_k\mathbf{x}_k + \mathbf{v}_k \tag{14}$$

There is a large overlap between the target area scanned by measurement $\mathbf{z}_k$ and the target area scanned by measurement $\mathbf{z}_{k+1}$, as depicted in Fig. 6. The extension to the front of the UAV seen by measurement $\mathbf{z}_{k+1}$ is predicted and the extension to the back of the UAV no longer seen by measurement $\mathbf{z}_{k+1}$ is omitted, with the rest of the target area carried over from state $\mathbf{z}_k$.
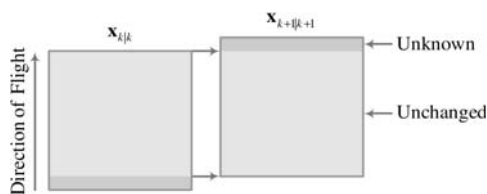

Fig. 6. Correlation between two states

As the target area is assumed to be static with a few slow moving objects on a stable background, the target area as seen by measurement $\mathbf{z}_k$ is assumed to be equal to the target area as seen by measurement $\mathbf{z}_{k+1}$. For the same reason the extension to the front on the UAV seen by measurement $\mathbf{z}_{k+1}$ is predicted to be equivalent to the target area just before this extension.

Mathematically this is done by shifting pixel rows $P^n\big|_{n=2,\ldots,N}$ of a posteriori state estimate $\mathbf{x}_{k|k}$ unchanged into pixel rows $P^n\big|_{n=1,\ldots,N-1}$ of a priori state estimate $\mathbf{x}_{k+1|k}$ and predicting pixel row P^N of state $\mathbf{x}_{k+1}$ as equal to pixel row P^N of state $\mathbf{x}_k$ using state evolution $\mathbf{A}_k$ defined as

$$\mathbf{A}_k = \begin{bmatrix} \mathbf{A}_k^{'} & \mathbf{0} & \mathbf{0} & \mathbf{0} \\ \mathbf{0} & \mathbf{A}_k^{'} & \mathbf{0} & \mathbf{0} \\ \mathbf{0} & \mathbf{0} & \ddots & \mathbf{0} \\ \mathbf{0} & \mathbf{0} & \mathbf{0} & \mathbf{A}_k^{'} \end{bmatrix} \quad \text{where} \quad \mathbf{A}_k^{'} = \begin{bmatrix} 0 & 1 & 0 & 0 \\ 0 & 0 & \ddots & 0 \\ 0 & 0 & 0 & 1 \\ 0 & 0 & 0 & 1 \end{bmatrix} \quad (15)$$

A posteriori state estimate $\mathbf{x}_{k|k}$ is initialised as $\mathbf{x}_{k|k}\big|_{k=0}=\mathbf{0}$, a $\mathbf{A}_k^{'}$ is required for each pixel column P^m and pixel columns P^m of state $\mathbf{x}_k$ are lexicographically ordered into one column for multiplication with state evolution $\mathbf{A}_k$.

The antenna concurrently scans the target area along the plane perpendicular to the flight path, with each orientation scanned by a beam at a different frequency f_0^m. The frequency range f_L to f_H is divided into $M=9$ contiguous bands, each assigned to a different pixel column, P^m. Even though the main beam at frequency f_0^m is orientated to a particular part of the target, the whole target area is measured at frequency f_0^m.

Therefore, the antenna patterns at the different frequencies f_0^m are combined to reconstruct the target area. Mathematically this is done by combining the $M=9$ measured 2D antenna patterns, Ant_{2D}, into one measurement evolution $\mathbf{H}_k$. Each row of measurement evolution $\mathbf{H}_k$ relates one frequency component of measurement $\mathbf{z}_k$ to state $\mathbf{x}_k$, as depicted in Fig. 7.
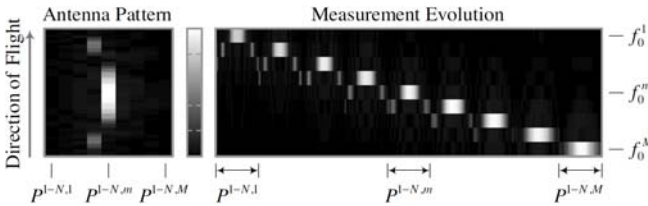

Fig. 7. Measurement model

As the antenna has a narrow beam along the plane perpendicular to the flight path, only pixel column P^m is significant affected by Ant_{2D}^m. As the antenna has a broad beam along the plane of the flight path, many pixels within pixel column P^m are significant affected by Ant_{2D}^m. This blurs the image, making it difficult to determine the position of objects or to differentiate between objects situated along the flight path.

The three covariance matrices are initialised as

$$\mathbf{P}_{k|k}\Big|_{k=0} = \mathbf{A}_k \epsilon_1 \mathbf{A}_k^T$$
$$\mathbf{Q}_k\Big|_{k=0} = \mathbf{A}_k \epsilon_2 \mathbf{A}_k^T \qquad (16)$$
$$\mathbf{R}_k\Big|_{k=0} = \mathbf{H}_k \epsilon_3 \mathbf{H}_k^T$$

where ϵ_1, ϵ_2 and ϵ_3 reflect the degree of uncertainty in the state, the measurement and the process.

Given the initial conditions of a posteriori state estimate $\mathbf{x}_{k|k}\big|_{k=0}$ and a posteriori state error covariance $\mathbf{P}_{k|k}\big|_{k=0}$, the Kalman filter is obtained iteratively by predicting the a priori estimates

$$\mathbf{x}_{k+1|k} = \mathbf{A}_k \mathbf{x}_{k|k} + \mathbf{B}_k \mathbf{u}_k$$
$$\mathbf{z}_{k+1|k} = \mathbf{H}_k \mathbf{x}_{k+1|k} \qquad (17)$$
$$\mathbf{P}_{k+1|k} = \mathbf{A}_k \mathbf{P}_{k|k} \mathbf{A}_k^T + \mathbf{Q}_k$$

and computing Kalman gain $\mathbf{K}_{k+1}$ to update the a posteriori estimates

$$\mathbf{K}_{k+1} = \mathbf{P}_{k+1|k} \mathbf{H}_{k+1}^T (\mathbf{H}_{k+1} \mathbf{P}_{k+1|k} \mathbf{H}_{k+1}^T + \mathbf{R}_{k+1})^{-1}$$
$$\mathbf{x}_{k+1|k+1} = \mathbf{x}_{k+1|k} + \mathbf{K}_{k+1}(\mathbf{z}_{k+1} - \mathbf{z}_{k+1|k}) \qquad (18)$$
$$\mathbf{P}_{k+1|k+1} = (\mathbf{I} - \mathbf{K}_{k+1}\mathbf{H}_{k+1})\mathbf{P}_{k+1|k}(\mathbf{I} - \mathbf{K}_{k+1}\mathbf{H}_{k+1})^T + \mathbf{K}_{k+1}\mathbf{R}_{k+1}\mathbf{K}_{k+1}^T$$

5. Results

Specific target areas are simulated to test the ability of the Kalman filter to model the flight process and to remove the blur of the measurement process. The input parameters are gradually increased from idealised values to the expected values to simplify the optimisation process.

As a first experiment, the ability of the Kalman filter to model the flight process is tested for a target area containing a single frequency component and with measurement evolution $\mathbf{H}_k$ of size 9×27 based on antenna measurements using a reflector that concentrates antenna pattern Ant_{2D} into a $1^\circ \times 1^\circ$ main beam, as depicted in Fig. 8. This idealisation removes the interfering effect of neighbouring frequency components and the blurring effect of the antenna pattern to simplify the problem to just one involving the modelling of the flight process.
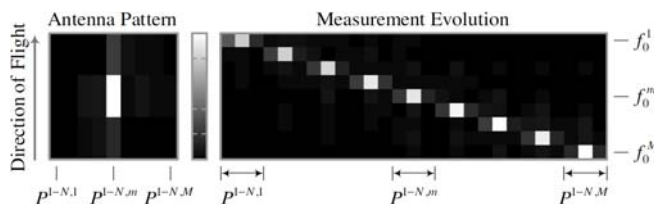

Fig. 8. Idealised measurement model

The response to the change between pixel row P^n and pixel row P^{n+1} is not quick enough, resulting in a delayed response in a posteriori state estimate $\mathbf{x}_{k|k}$ to state $\mathbf{x}_k$, as depicted in Fig. 9. An improved response is obtained by adding a velocity parameter Δx_k to state $\mathbf{x}_k$ that calculates the change between pixel row P^{N-1} and pixel row P^N.
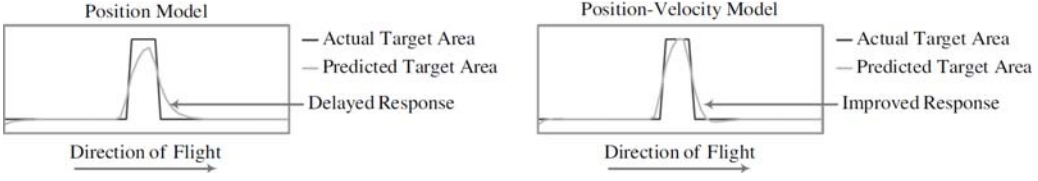
Fig. 9. Idealised Single Frequency Target Area

For this position-velocity model pixel row P^N of state $\mathbf{x}_{k+1}$ is predicted as the sum of pixel row P^N of state $\mathbf{x}_k$ and the change between pixel row P^{N-1} and pixel row P^N of state $\mathbf{x}_k$ and the change between pixel row P^{N-1} and pixel row P^N of state $\mathbf{x}_{k+1}$ is equated with the change between pixel row P^{N-1} and pixel row P^N of state $\mathbf{x}_k$ using state evolution $\mathbf{A}_k$

$$\mathbf{A}_k = \begin{bmatrix} \mathbf{A}'_k & \mathbf{0} & \mathbf{0} & \mathbf{0} \\ \mathbf{0} & \mathbf{A}'_k & \mathbf{0} & \mathbf{0} \\ \mathbf{0} & \mathbf{0} & \ddots & \mathbf{0} \\ \mathbf{0} & \mathbf{0} & \mathbf{0} & \mathbf{A}'_k \end{bmatrix} \quad \text{where} \quad \mathbf{A}'_k = \begin{bmatrix} 0 & 1 & 0 & 0 & 0 \\ 0 & 0 & \ddots & 0 & 0 \\ 0 & 0 & 0 & 1 & 0 \\ 0 & 0 & 0 & 1 & 1 \\ 0 & 0 & 0 & 0 & 1 \end{bmatrix} \tag{19}$$

With no correlation between the velocity parameter Δx_k of state $\mathbf{x}_k$ and measurement $\mathbf{z}_k$, measurement evolution $\mathbf{H}_k$ of Fig. 8 is altered to a form of size 9×36 by inserting a zero-value column after each pixel column P^m, as depicted in Fig. 10.
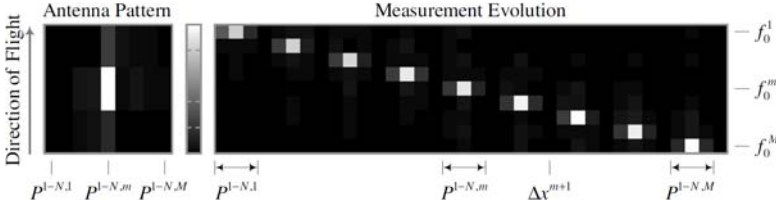

Fig. 10. Idealised measurement model using position-velocity model

A second experiment is performed to test the ability of the Kalman filter to model the flight process for the same target area, but this time with measurement evolution $\mathbf{H}_k$ of size 9×108 based on antenna measurements using a reflector that concentrates antenna pattern Ant_{2D} into a $1^\circ \times 10^\circ$ main beam, as depicted in Fig. 11. The idealisation of the measurement model is lessened to incorporate modelling of the blurring effect of the antenna pattern. The increased width of the main beam maps onto a larger surface than the $1^\circ \times 1^\circ$ main beam, requiring a larger measurement evolution $\mathbf{H}_k$ to model the relationship between state $\mathbf{x}_k$ and measurement $\mathbf{z}_k$.
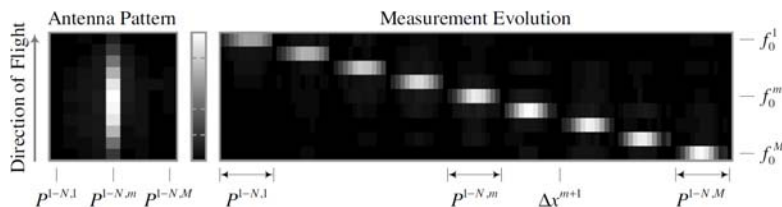
Journal of the Serbian Society for Computational Mechanics / Vol. 4 / No. 1, 2010

Fig. 11. Partially idealised measurement model

The response to the change between pixel row P^n and pixel row P^{n+1} of state $\mathbf{x}_k$ is spread over a number of pixels proportional to the width of the main beam, resulting in a blurred response in a posteriori state estimate $\mathbf{x}_{k|k}$ to state $\mathbf{x}_k$, as depicted in Fig. 12. An improved response is obtained by increasing the number of time steps calculated per Kalman filter loop.
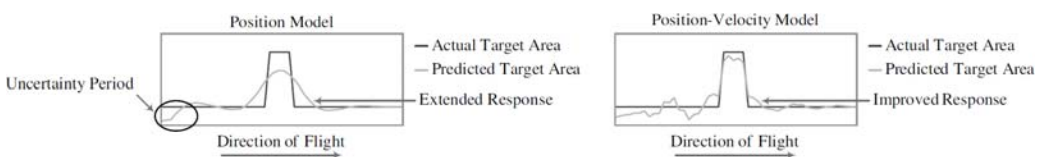

Fig. 12. Partially idealised single frequency target area

For this multi-measurement model state $\mathbf{x}_k$ is extended by c pixel rows, where c is the number of extra time steps calculated per Kalman filter loop, which extends the size of each $\mathbf{A}_k'$ by c in state evolution $\mathbf{A}_k$.

For this multi-measurement model the rows within measurement evolution $\mathbf{H}_k$ are repeated c times, but with a one pixel offsets due to the shift in focus from time step k to time step $k+1$, as depicted for measurement evolution $\mathbf{H}_k$ of size 9×198 with $c = 10$ in Fig. 13.
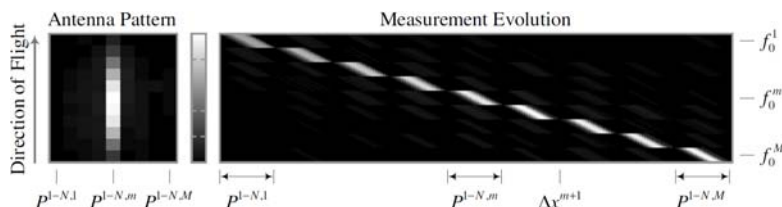

Fig. 13. Partially idealised measurement model using multi-measurement model

The size of measurement evolution $\mathbf{H}_k$ has a direct effect on the number of time steps the Kalman filter takes to adapt to the model. The larger the area the main beam of antenna pattern Ant_{2D} maps onto, the more pixels that need to be predicted concurrently in the initialisation of a posteriori state estimate $\mathbf{x}_{k|k}\,|_{k=0}$ and the longer the uncertainty period of a posteriori state estimate $\mathbf{x}_{k|k}$. The uncertainty period for the $1° \times 10°$ main beam is longer than for the $1° \times 1°$ main beam, as depicted in Fig. 12.

The reason for the improved response of the multi-measurement model is accredited to the increased size of measurement evolution $\mathbf{H}_k$. For a single time step per Kalman filter loop and a single frequency component target area, the denominator of the Kalman gain $\mathbf{K}_k$ of (8) is a 1×1 matrix that can only globally rectify the Kalman gain $\mathbf{K}_k$ of size 12×1, and thereby only globally rectify the pixels of state $\mathbf{x}_k$.

When the number of time steps is increased per Kalman filter loop to 11 with $c = 10$, the denominator of the Kalman gain $\mathbf{K}_k$ of (8) increases in size to 11×11. In approaching the size of the Kalman gain $\mathbf{K}_k$ of 22×11, the elements of Kalman gain $\mathbf{K}_k$ are rectified individually and thereby the pixels of state $\mathbf{x}_k$ are rectified individually. Only when a large number of time steps are used per Kalman filter loop does $\mathbf{K}_k \rightarrow \mathbf{H}_{k+1}^{-1}$ when $\mathbf{R}_{k+1} \rightarrow \mathbf{0}$.

The final set of experiments test the ability of the Kalman filter to remove the errors in the measurement process using measurement evolution $\mathbf{H}_k$ of Fig. 13 and a full frequency range target area of size 9×50 containing a single central high intensity object of size 3×3 surrounded by a low intensity background, as depicted in Fig. 14. The last idealisation is removed to incorporate modelling of the interfering effect of neighbouring frequency components. The large size of measurement evolution $\mathbf{H}_k$ results in a long uncertainty period.
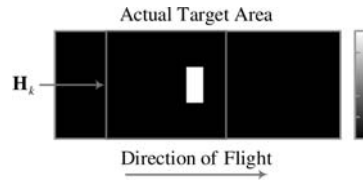

Fig. 14. Partially Idealised Full Target Area with Single Object

The variance in absolute gain between the $M = 9$ components of antenna pattern Ant_{2D} returns a false multi-level object and background, while the partial blurring of the object to neighbouring bands is accredited to non-ideal slope of the main beam. The Kalman filter is able to reduce both of these inaccuracies once the long uncertainty period has past, as depicted in Fig. 15.
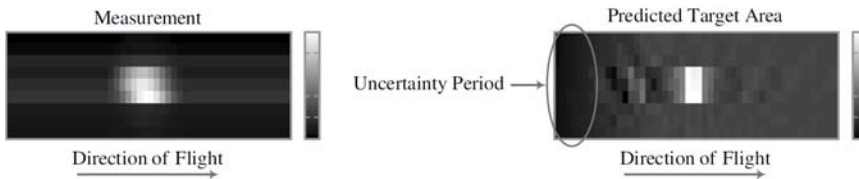

Fig. 15. Predicted Target Area for Partially Idealised Full Target Area with Single Object

The ability of the Kalman filter to differentiate between objects situated along the plane of the flight path is tested using the same measurement evolution $\mathbf{H}_k$ of Fig. 13, but this time with a full frequency range target area of size 9×50 containing a single central high intensity object of size 3×3 bordered by two moderately high objects of size 7×7 and surrounded by a low intensity background, as depicted in Fig. 16.
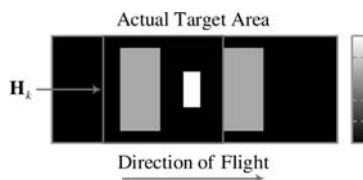
Fig. 16. Partially Idealised Full Target Area with Multiple Objects

The ability of the Kalman filter to reduce the variance in absolute gain between the $M = 9$ components of antenna pattern Ant_{2D} and the infringement of the main beam into neighbouring bands is not affected by the number of objects within the target area. The blurring effect of antenna pattern Ant_{2D} merges the closely spaced objects into a single object, with a false higher intensity at the location of the two border objects. The Kalman filter is able to response quick enough to a change between pixel row P^n and pixel row P^{n+1} of state $\mathbf{x}_k$, resulting in the objects being individually sharpened and detached from each other, as depicted in Fig. 17.
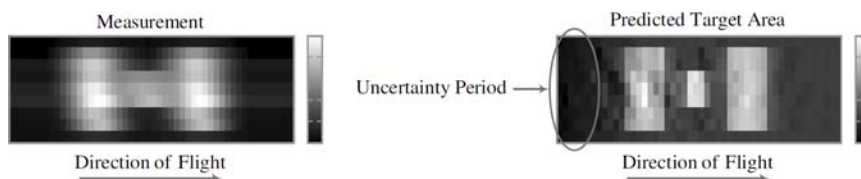

Fig. 17. Predicted target area for partially idealised full target area with multiple objects

6. Conclusions

Advances in UAV technology have created the option of introducing PMMW imaging capability into an autonomous vehicle for low-visibility conditions. However, the size of the UAV places restrictions on the design of the system in the inability to incorporate any measure to focus the antenna pattern before image creation that leads to a non-ideal antenna pattern.

A technique is needed to reconstruct the image after image creation. Conventional image reconstruction processes deal with localised object blurring modelled by Gaussian noise, which is insufficient to counter the more global object blurring of the antenna pattern, and are designed for stationary stand-alone images.

This paper proposes a new unconventional technique based on the Kalman filter. For each time-interval the Kalman filter makes a prediction of the detected signal using the measured antenna pattern. The comparison between the predicted signal and the detected signal is used to generate an accurate image of the target area.

The Kalman filter corrects unequal gain between frequency components, reduces blur into other frequency components and other time intervals and separate closely spaced objects for a partially focused beam measuring a simulated target area. It remains to be proven whether the Kalman filter is functional for an unfocused beam measuring an actual target area.

References

Alvarez L, Mazorra L (1994). Signal and Image Restoration Using Shock Filters and Anisotropic Diffusion, *SIAM Journal on Numerical Analysis*, 31(2), 590-605.

Andrade-Cetto, J (2005). The Kalman Filter, *Tech Rep IRI-DT-02-01*, Institut de Robótica i Informática Industrial, Universitat Politécnica de Catalunya, Barcelona, Spain.

Appleby R, Anderton RN (2007). Millimeter-Wave and Submillimeter-Wave Imaging for Security and Surveillance, *Proceedings of the IEEE*, 95(8), 1683-1690.

Chandrasekar V, Fukatsu H, Mubarak K (2003). Global Mapping of Attenuation at Ku- and Ka-Band, *IEEE Transactions on Geoscience and Remote Sensing*, 41(10), 2166-2176.

Gilboa G, Sochen N, Zeevi YY (2003). Texture Preserving Variational Denoising Using an Adaptive Fidelity Term, *Proceedings of the VLSM*, 137-144.

Hopper R (2005). System Solutions using MMW Sensors, *Proceedings of ARMMS*.

Kalman RE (1960). A New Approach to Linear Filtering and Prediction Problems, *Transactions of the ASME - Journal of Basic Engineering*, 82(Series D), 35-45.

Liebe HJ (1983). Atmospheric EHF Window Transparencies near 35, 90, 140, and 220 GHz, *IEEE Transactions on Antennas and Propagation*, 31(1), 127-135.

Osher S, Rudin LI (1990). Feature-Oriented Image Enhancement Using Shock Filters, *SIAM Journal on Numerical Analysis*, 27(4), 919-940.

Perona P, Malik J (1990). Scale-Space and Edge Detection Using Anisotropic Diffusion, *IEEE Transactions on Pattern Analysis and Machine Intelligence*, 12(7), 629-639.

Rudin LI, Osher S, Fatemi E (1992). Nonlinear Total Variation Based Noise Removal Algorithms, *Physica D: Nonlinear Phenomena*, 60, 259-268.

Ulaby FT, Moore RK, Fung AK (1986). *Microwave Remote Sensing*, 3, Artech House, USA.

Wilson WJ, Howard RJ, Ibbot AC, Parks GS, Ricketts WB (1986). Millimeter-Wave Imaging Sensor, *IEEE Transactions on Microwave Theory and Techniques*, 34(10), 1026-1035.

Yujiri L (2003). Passive Millimeter-Wave Imaging, *IEEE Microwave Magazine*, 4(3), 39-50.